

Effects of Hydrogen and Hydrothermal Pretreatments on a Silica-Supported Copper Catalyst for CO Oxidation: Copper Hydroxy Active Species

Miao-Miao Wang, Jing Yu, Wei-Wei Wang, Jun-Xiang Chen, Chun-Jiang Jia,* and Rui Si*

Cite This: *J. Phys. Chem. C* 2020, 124, 25270–25281

Read Online

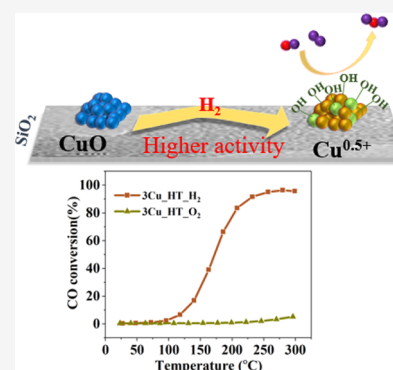
ACCESS |

Metrics & More

Article Recommendations

Supporting Information

ABSTRACT: As an inert support, silica is appropriate to disperse active copper species to study the intrinsic structure–activity relationship for redox reactions including CO oxidation. Herein, a copper–silica catalyst (3 wt % Cu) was synthesized via a deposition–precipitation method, followed by a hydrogen and/or hydrothermal treatment. The sequential CO oxidation tests over the as-calcined samples show that the hydrothermal treatment effectively promoted the catalyst stability of Cu/SiO₂. Hydrogen treatment can significantly increase CO conversion compared to oxygen treatment whose conversion rates are less than 10%. Multiple structural characterizations, including temperature-programmed reduction by hydrogen, temperature-programmed reduction by CO, X-ray absorption fine structure, and in situ diffuse reflectance infrared Fourier transform spectroscopy, were used to precisely determine the active species of small-sized copper catalysts. These analyses identify that the textural structure of silica and the coordination environment of the copper oxide species changed after the hydrothermal treatment, which make the catalysts more stable. The hydrogen pretreatment not only reduced copper oxide but also generated the copper hydroxyl species to make the adsorption of the CO reactant much easier. This work demonstrates the importance of hydrogen pretreatment in enhancing the catalytic activity of copper catalysts and the crucial role of copper hydroxyl groups in CO oxidation reactions for Cu-based catalysts.



1. INTRODUCTION

CO oxidation, as a prototypical reaction, has long been applied to fundamental research and industrial applications. Until now, noble metal catalysts including Pt, Pd, Ru, Rh, Au, and Ir have been systematically studied for CO catalytic oxidation because of their well-known superior catalytic performances.^{1–3} However, high cost limited the availability of noble metal catalysts, which is a driving force for finding alternatives to noble metals. Transition metal catalysts as a kind of non-noble metal catalysts such as Co, Cu, Mn, Ni, and so forth are increasingly being investigated for CO oxidation.^{4,5} Among them, Cu-based catalysts, belonging to the same elemental group as Au, have been investigated on the CO oxidation reaction.

At present, there are many studies on the influence of copper valency,^{6,7} size,⁸ crystal plane effect,^{6,9} shape,^{10,11} adjunct,¹² pretreatment conditions, and reaction conditions¹³ on CO oxidation activity. Dynamic studies and the structure–activity relationship of copper in the CO oxidation reaction have been getting more and more attention. On the one hand, it can be found that reducible supports such as CeO₂ and ZnO₂ are widely favored by researchers because they have variable oxidation states and strong interactions with copper, which have a remarkable promotion effect for catalytic activity in many research results.^{14–16} On the other hand, in order to

evaluate the relationship between the catalytic activity and the intrinsically active sites of Cu nanoparticles exactly, SiO₂ as an inert support devoid of the possibility of participating into the CO oxidation reaction has been used by researchers to deposit copper nanoparticles.¹⁷

It is well known that the conditions and methods for preparing catalysts are critical to catalytic activity. The hydrothermal method, a simple and mature synthesis technique, has been widely used to prepare materials such as metal oxide supports^{4,18} and multivalent solid–solution supports.¹⁹ Hydrothermal treatment of the catalysts has been shown to improve the catalytic performance by changing the physicochemical properties of the materials,^{20,21} introducing hydroxyl groups,^{22,23} and so forth. Mironenko found that the fraction of surface bridging OH groups and the concentration of Lewis acid sites were increased in γ -Al₂O₃ by the hydrothermal treatment and the subsequently prepared Pt/ γ -Al₂O₃ catalyst promoted the *n*-hexane transformations and

Received: August 3, 2020

Revised: October 18, 2020

Published: November 6, 2020



propane dehydrogenation.²² Jiang group synthesized the multiwalled carbon nanotubes bearing hydroxyl groups on the exterior surface by an alkaline-mediated hydrothermal treatment method.²³ In addition, hydrogen pretreatment was mostly used for silica-supported copper catalysts for CO oxidation reactions.^{6,7,17,24} Tu et al. said that it was not clear why reduction treatment is required for obtaining the high activity on the Cu particles.¹⁷ It is generally believed that hydrogen pretreatment reduced copper species to metallic copper that was considered to be much more active than the copper oxides. Perhaps there are other effects of hydrogen pretreatment of the catalytic system that have not been discovered.

In this work, we used a simple deposition–precipitation method to prepare a 3 wt % Cu/SiO₂ catalyst without additives. We introduced the hydrothermal and hydrogen pretreatment steps to enhance the catalytic performance on CO oxidation. Subsequently, the effect of these pretreatment conditions on the structure and catalytic activity of the catalysts was explored, which elaborates the important role of copper hydroxyls in CO oxidation.

2. EXPERIMENTAL SECTION

2.1. Catalyst Preparation. All the chemicals are of analytical grade and were used without further purification or modification. Silicon dioxide was obtained from Evonik Specialty Chemicals (Shanghai) Co., Ltd. Copper nitrate (Cu(NO₃)₂·3H₂O) and sodium carbonate (Na₂CO₃, 99.8%) were purchased from Sinopharm Chemical Reagent Co., Ltd.

The Cu-supported SiO₂ catalysts were prepared by the deposition–precipitation method. Copper nitrate blue crystals and sieved (100 mesh) silicon dioxide powders were added into 70 mL of deionized H₂O (18.2 MΩ·cm) under vigorous stirring on a Teflon-lined stainless steel autoclave (inner volume: 100 mL). Then, Na₂CO₃ aqueous solution (0.25 M) was added into the suspension dropwise until the final pH value of 10. The alkaline suspension was further stirred at room temperature for 2 h for aging. The aged suspension was subsequently hydrothermally heated at 200 °C for 24 h. After the hydrothermal process was finished and the vessel was cooled down to room temperature, the precipitates were collected by suction filtration using a Brinell funnel and washed by deionized water until neutral. The product was dried under vacuum at 80 °C overnight and then calcined in air at 400 °C for 4 h (2 °C·min⁻¹). The calcined Cu/SiO₂ samples were denoted as 3Cu-HT. Pure SiO₂ with no copper added after the hydrothermal step is marked as SiO₂-HT.

The preparation steps of 3Cu catalysts are almost the same as that of 3Cu-HT except that the hydrothermal process is not done. Similarly, pure SiO₂ with no copper added is marked as SiO₂.

The samples pretreated by H₂ were marked as 3Cu-HT-H₂ or 3Cu-H₂. Similarly, the samples pretreated by O₂ were marked as 3Cu-HT-O₂ or 3Cu-O₂. The samples after CO oxidation are marked (used). For example, after CO oxidation, 3Cu-HT-H₂ is marked as 3Cu-HT-H₂ (used).

2.2. Characterization. The copper contents were detected by inductively coupled plasma atomic emission spectroscopy (ICP–AES) on an Optima 5300DV (PerkinElmer Co.). The as-calcined powder sample (100 mg) was dissolved completely in 2 mL of hydrofluoric acid. For eliminating silica in the form of SiF₄, the solution was evaporated to near dry. Then, 3 mL of nitric acid was added and shaken. The solution was slightly

boiled for ca. 2 h subsequently. Finally, the abovementioned solution was cooled down to room temperature and diluted with high-purity water for ICP–AES test.

The diffraction patterns of catalysts were tested by Bruker AXS D2 PHASER using Cu Kα radiation ($\lambda = 0.15406$ nm) and calibrating the 2θ angles with a micrometer-scale alumina disc. After grinding, the catalyst was flattened on a quartz glass sample holder before each testing. The diffraction patterns were collected from 10 to 90° with a step of 0.08°.

The transmission electron microscopy (TEM) and high-resolution TEM (HRTEM) images were obtained from a FEI Tecnai F20 microscope operating at 200 kV. After suspending fully by manually shaking in ethanol liquid, one drop of catalyst suspension was dropped on an ultrathin carbon film-coated Mo grid using a pipette. The as-prepared sample was dried naturally before placing on the TEM sample holder.

The nitrogen adsorption/desorption characterization was performed on an ASAP2020-HD88 analyzer (Micromeritics Co., Ltd., Atlanta, GA, USA) at 77 K for testing the Brunauer–Emmett–Teller (BET) specific surface area and pore size distribution of the samples. Before analyzing under the N₂ atmosphere cooling with liquid nitrogen, the samples were degassed at 250 °C under vacuum conditions over 4 h. The calculation of pore size (D_p) distribution is determined by the Barrett–Joyner–Halenda (BJH) method from the desorption branch of the isotherms. The BET specific surface areas (S_{BET}) were obtained from the data of the relative pressure between 0.05 and 0.20.

N₂O chemisorption measurements were carried out in a Builder PCSA-1000 instrument with a thermal conductivity detector (TCD) to detect the amount of H₂ consumption for evaluating the dispersion of copper catalysts. The sieved catalysts (20–40 mesh, 50 mg) were placed into a heat-resistant U-type tube and underwent three sequential steps. Step 1 represents the reduction of CuO by H₂, CuO + H₂ → Cu + H₂O. The catalysts were oxidized by a high-purity oxygen gas (99.999%) at 300 °C for 0.5 h and then cooled to room temperature with He (30 mL·min⁻¹). The catalyst was reduced by 5% H₂/He (30 mL·min⁻¹) from room temperature to an elevated opportune temperature (10 °C·min⁻¹). The amount of H₂ consumption (A_1) corresponds to the total amount of CuO. Step 2 represents the oxidation of surface Cu to Cu₂O by N₂O, 2Cu + N₂O → Cu₂O + N₂. In this step, the reduced catalyst was cooled to 35 °C purging with He (30 mL·min⁻¹), which took 1 h. Then, 5% N₂O/Ar (40 mL·min⁻¹) was introduced to oxidize Cu at 35 °C for 1 h. Step 3 represents a reduction of surface Cu₂O species, Cu₂O + H₂ → 2Cu + H₂O. First, the catalyst was also purged with He (30 mL·min⁻¹) for 0.5 h to remove the residual N₂O. Subsequently, 5% H₂/He (30 mL·min⁻¹) was introduced to reduce Cu₂O from room temperature to 500 °C (10 °C·min⁻¹). The amount of H₂ consumption (A_2) corresponds to the amount of Cu₂O. The dispersion (D) of CuO was calculated as $D = 2A_2/A_1 \times 100\%$.

H₂-temperature programmed reduction (H₂-TPR) measurement of the sample was carried out on a Micromeritics AutoChem 2920. Before measurement, the sieved fresh sample (100 mg, 20–40 mesh) was pretreated in 5% O₂/Ar (30 mL·min⁻¹) at 300 °C for 30 min and then cooled down to room temperature in the same gas. After purging with He (50 mL·min⁻¹) for 15 min to remove the residual oxygen, the catalyst was heated from room temperature to 500 °C in continuous 5% H₂/He (30 mL·min⁻¹, 10 °C·min⁻¹). The amount of H₂ consumption was detected by a TCD.

X-ray absorption fine structure (XAFS) spectroscopy at the Cu K-edge ($E_0 = 8979$ eV) was performed at the BL14W1 beamline of Shanghai Synchrotron Radiation Facility (SSRF) operated at 3.5 GeV under the “top-up” mode with a constant current of 220 mA. The sample mixing the LiF powders uniformly was flattened into a sheet using a tableting machine and then sealed with a Kapton tape. The XAFS data were recorded under the transmission mode. The energy was calibrated with the absorption edge of the Cu foil as a reference. Athena and Artemis codes were used to extract the data and fit the profiles. For the X-ray absorption near-edge spectroscopy (XANES) part, the experimental absorption coefficients as a function of energy $\mu(E)$ were processed by background subtraction and normalization procedures and reported as “normalized absorption”. Based on the normalized XANES profiles, both the molar proportion of $\text{Cu}^{2+}/\text{Cu}^0$ and the oxidation state of Cu can be determined by the linear combination fit with the help of various references (Cu foil for Cu^0 and CuO for Cu^{2+}). For the extended XAFS (EXAFS) part, the Fourier transformed data in the R space were analyzed by applying CuO and a metallic Cu model for Cu–O and Cu–(O)–Cu contributions. The passive electron factors, S_0^2 , were determined by fitting the experimental data on Cu foils and setting the coordination number (CN) of Cu–Cu to be 12 and then fixed for further analysis of the measured samples. The parameters describing the electronic properties (e.g., correction to the photoelectron energy origin, E_0) and the local structure environment including the CN, bond distance (R), and Debye–Waller factor around the absorbing atoms (σ^2) set as 0.0045 and 0.008 for O and Cu, respectively, for all samples except 3Cu-HT-H₂. For 3Cu-HT-H₂, the Debye–Waller factor around the absorbing atoms (σ^2) set as 0.003 and 0.008 Å² for O and Cu, respectively. The fitted ranges for K and R spaces were selected to be $k = 2.5\text{--}11.5$ Å^{−1} for all samples.

In situ diffuse reflectance infrared Fourier transform spectroscopy (in situ DRIFTS) was employed to study the surface adsorption. The catalyst powder was placed into a diffuse reflectance cell (Harrick system) equipped with CaF₂ windows on a Bruker Vertex 70 spectrometer using a mercury–cadmium–telluride detector cooled with liquid nitrogen. A “CO–He–CO–O₂” test was done for investigation of the process of adsorption/desorption of CO over Cu/SiO₂ catalysts. The powder sample (20 mg) was pretreated in synthetic air (21% O₂/N₂) or 5% H₂/He at 300 °C for 30 min and cooled to room temperature under the same gas (30 mL·min^{−1}). After purging with He (30 mL·min^{−1}) for 20 min to remove the pretreatment gas, a background spectrum was collected via 32 scans at 4 cm^{−1} resolution at 30 °C under pure He (30 mL·min^{−1}) until repetitive spectrum. Subsequently, the gas with 2% CO/He was introduced into the in situ chamber (30 mL·min^{−1}) for CO adsorption for 30 min, collecting 40 independent spectra during this process. He steam was subsequently admitted, instead of CO, for purging for 30 min, also corresponding to 40 IR spectra. Then, the catalyst was exposed to 2% CO/He for CO readsorption for 30 min. Ultimately, 1% O₂/N₂ stream was introduced in order to investigate the surface changes during the CO removal process. DRIFTS spectra were obtained by subtracting the background spectrum from the subsequent spectra. The spectra were analyzed using OPUS software.

CO-temperature programmed reduction (CO-TPR) was carried out in a Micromeritics AutoChem 2920, and gas signals were collected by using a mass spectrometer (TILON GRP

TECHNOLOGY LIMITED, LC-D200M). Before testing, the as-prepared sample (100 mg, 20–40 mesh) was pretreated in 5% H₂/He or 5% O₂/Ar (30 mL·min^{−1}) at 300 °C for 30 min and then cooling down to room temperature under the same steam. He (50 mL·min^{−1}) was introduced for purging for 20 min. The He steam was switched to 5% CO/He later and the sample was heated from room temperature to 500 °C with a step of 10 °C·min^{−1}. The signals of H₂ ($m/z = 2$), He ($m/z = 4$), and CO₂ ($m/z = 44$) were detected during the investigation. The detected data was normalized by dividing the He signal ($m/z = 4$).

2.3. Catalytic Tests. CO oxidation reactions were carried out in a Micromeritics AutoChem 2920. The sieved sample (40–60 mesh, 100 mg) was placed into a U-shaped quartz tube and then preactivated with 5% H₂/He or 5% O₂/N₂ for 30 min (50 mL·min^{−1}) before the reaction testing. Pure He gas was used to purge H₂ or O₂ for 20 min after the sample was cooled to room temperature. Afterward, the CO oxidation reaction of the Cu/SiO₂ catalyst was measured in stoichiometric gas of 2% CO/1% O₂/97% He (30 mL·min^{−1}) corresponding to a gas hourly space velocity (GHSV) of 18,000 mL·h^{−1}·g_{cat}^{−1}. The temperature began from 30 to 300 °C with a heating rate of 10 °C·min^{−1} in succession and the outlet gas compositions were recorded every 2.5 min on-line by Micro GC Fusion gas chromatography (INFICON Company). The stability tests were done in the same conditions at a constant reaction temperature of 200 °C for 700 min. The CO conversion of CO oxidation was calculated according to the following equation: CO conversion (%) = $(\text{CO}_{\text{in}} - \text{CO}_{\text{out}})/\text{CO}_{\text{in}} \times 100$.

3. RESULTS

3.1. CO Oxidation Reactivity of Copper–Silica Catalysts. The “light-off” profile of Cu-based catalysts is exhibited in Figure 1. Above all, the 3Cu/SiO₂ sample

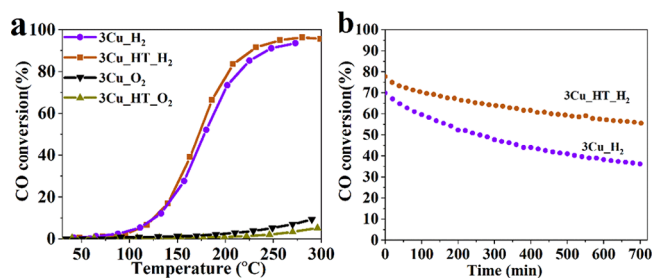


Figure 1. CO oxidation conversion over 3Cu/SiO₂ samples for (a) “light-off” experiments from 30 to 300 °C and (b) stability test at 200 °C. Reaction conditions: 2% CO/1% O₂/97% He and a GHSV of 18,000 mL·h^{−1}·g_{cat}^{−1}.

pretreated with H₂ shows significantly high CO conversions, whereas catalysts pretreated with O₂ are nearly inactive for CO oxidation (below 10% CO conversion at 300 °C) in the temperature range of 30–300 °C (Figure 1a). Interestingly, the hydrothermal step during sample preparation affects the performance of the catalyst, which is specifically manifested by the fact that the hydrothermal catalyst is more active than the nonhydrothermal catalyst. The comparison of the reactivity between hydrothermal and nonhydrothermal samples is inconspicuous on the transient profiles of CO conversion, only about 10 °C difference at 50% conversion. However, stability tests of 3Cu/SiO₂ reflected the advantage of the

hydrothermal step in Figure 1b. The conversion rate at the first point was 70% and the last point (720 min) conversion rate was 36% for 3Cu_H₂ corresponding to about 48% deactivation. The conversion rate at the first point was 78% and the last point (720 min) conversion was 56% for 3Cu_HT_H₂ corresponding to about 28% deactivation. In summary, the hydrogen pretreatment promoted the catalytic performance of copper–silica catalyst much more effectively than the hydrothermal pretreatment.

3.2. Structural and Textural Properties of Fresh Copper–Silica Catalysts.

Table 1. Cu Concentration, BET Specific Surface Areas (S_{BET}), and BJH Pore Volume (V_{p}) of SiO₂ Support and Size (D_{TEM}) of Cu

sample	Cu loading (wt %) ^a	S_{BET} (m ² ·g ⁻¹) ^b	V_{p} (cm ³ ·g ⁻¹) ^b	D_{TEM} (nm) ^c
SiO ₂		126	0.939	
SiO ₂ _HT		72	0.628	
3Cu	3.3	186	0.910	2.0 ± 0.5
3Cu_HT	3.7	121	0.824	2.3 ± 0.7
3Cu_HT_H ₂ (used)				2.5 ± 0.7
3Cu_HT_O ₂ (used)				2.4 ± 0.6

^aDetermined by ICP. ^bFrom N₂ adsorption/desorption. ^cStatistic data on the basis of TEM images.

show that the experimental Cu contents of 3Cu and 3Cu_HT are 3.3 and 3.7 wt %, respectively, which are close to the target value (3 wt %). The X-ray diffraction (XRD) patterns for the calcined catalysts in Figure 2a present only one broad peak at

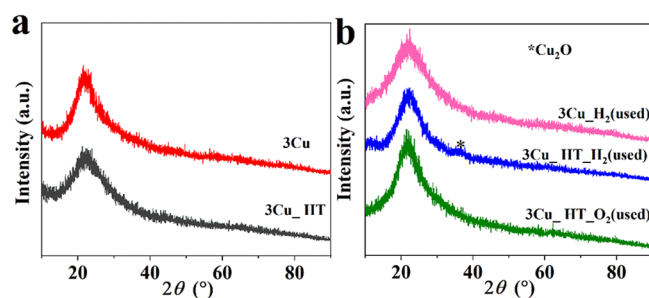


Figure 2. XRD patterns of 3Cu/SiO₂: (a) fresh samples and (b) used samples.

$2\theta \approx 22^\circ$ for 3Cu and 3Cu_HT, corresponding to amorphous silica support, indicating that the copper species are highly dispersed on the SiO₂ surface or small copper size is beyond the limitation of XRD detection in the fresh samples.

The textural properties of 3Cu/SiO₂ catalysts investigated by the nitrogen adsorption/desorption experiments are included in Figure 3 and Table 1. As shown in Figure 3a, the representative nitrogen adsorption/desorption isotherms of samples before and after hydrothermal treatment exhibit type IV isotherms for pure SiO₂ and Cu-doped catalysts. The original SiO₂ represents hysteresis loop H1 with the parallel hysteresis branches, indicating the absence of pore plugging by oxide nanoparticles.^{24,25} After deposition of Cu, 3Cu exhibits that the hysteresis loop changes from H1 to H2 type in the P/P_0 range of 0.8–1.0, revealing the partial disordering of the mesostructure.²⁴ Furthermore, 3Cu and SiO₂ show a hysteresis loop with an apparent plateau at high P/P_0 , giving a hint on uniform pore size distribution in nonhydrothermal catalysts.²⁶

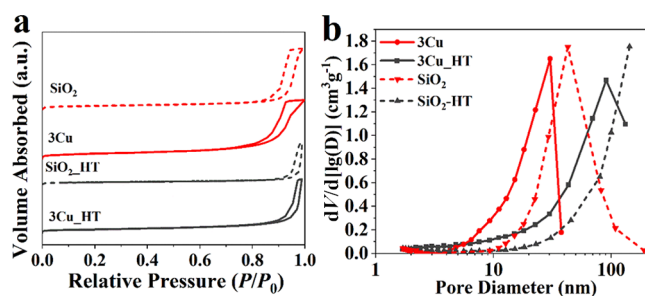


Figure 3. (a) N₂ adsorption/desorption isotherm and (b) BJH pore size distribution plots of 3Cu/SiO₂ and SiO₂.

After the hydrothermal step, these samples showed the absence of a plateau-like region or an inapparent plateau, showing that the hydrothermal materials contain both mesopores and macropores. The isotherms display the forced closure of the desorption branch at $P/P_0 > 0.8$ for all the samples, illustrating the absence of micropores.²⁷ However, the relative pressure associated with the capillary condensation of samples with the hydrothermal step shifted to higher values in comparison with the nonhydrothermal samples, indicating that the materials possess a larger pore size after hydrothermal treatment. This is evidenced by the BJH pore size distribution plots in Figure 3b and Table 1. The significant changes in either the isotherm or hysteresis shape/position reveal the modification of the topology of the mesopores and the alteration of the ordered mesoporous structure after the hydrothermal step. The BET specific surface areas and pore volumes of fresh samples summarized in Table 1 are distinct between 3Cu_HT (121 m²·g⁻¹, 0.824 cm³·g⁻¹) and 3Cu (186 m²·g⁻¹, 0.910 cm³·g⁻¹). Obviously, the hydrothermal step reduces the specific surface area and pore volume of the catalysts, which is also reflected on the pure SiO₂. These nitrogen adsorption/desorption experiments can be summarized that the hydrothermal step can markedly modify the textural properties of SiO₂.

3Cu/SiO₂ catalysts were tested for further morphological characterization by TEM in Figure 4. Comparing the TEM images of fresh 3Cu and 3Cu_HT in Figure 4a,c, after hydrothermal treatment, the size of the SiO₂ support was obviously enlarged, indicating that the hydrothermal process drove SiO₂ particles to merge to form a bigger wormlike structure. An increase in the support size was responsible for the decrease in BET specific surface area. HRTEM was carried out for observing the size of copper particles because of the fact that the characterization of Cu particles was difficult to perform by XRD. The average copper size on 3Cu is 2.0 ± 0.5 nm detected by HRTEM (Figure 4b). After hydrothermal treatment, the average size of the copper nanoparticles is 2.3 ± 0.7 nm (Figure 4d), which revealed that hydrothermal treatment almost had no effect on the size of copper. The results of TEM verified the experimental analysis of the N₂ adsorption/desorption, which indicates that hydrothermal treatment during preparation did affect the texture of the catalyst.

3.3. Reducibility and Local Coordination Structure of Copper–Silica Catalysts. In Figure 5a, the results of H₂-TPR for 3Cu and 3Cu_HT are shown. The experimental and theoretical uptakes of H₂ are estimated and summarized in Table 2. Consumptions of H₂ are calculated as a stoichiometric ratio on the basis of CuO reduced to Cu. The only peak of both 3Cu and 3Cu_HT can be ascribed to reduction of highly

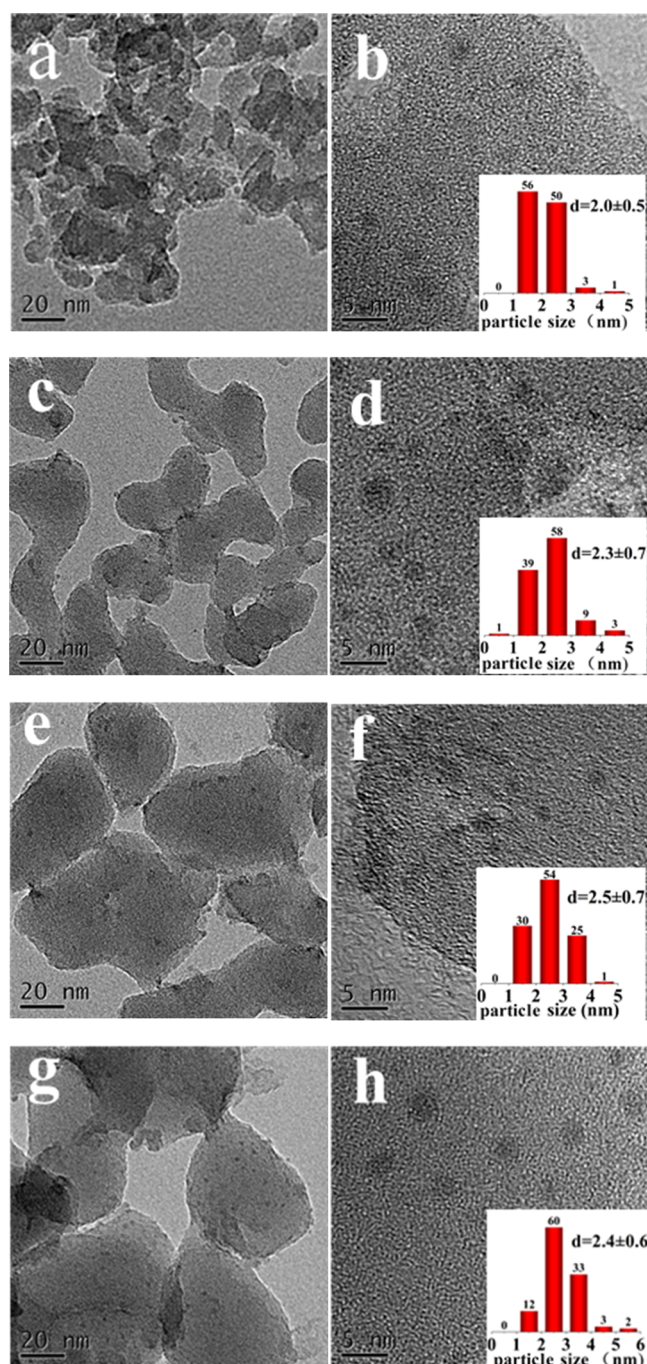


Figure 4. TEM (a,c,e,g) and HRTEM (b,d,f,h) images of 3Cu/SiO₂ samples: (a,b) 3Cu, (c,d) 3Cu_{HT}, (e,f) 3Cu_{HT}H₂(used), and (g,h) 3Cu_{HT}O₂(used). Insets show the corresponding size distribution of Cu.

dispersed small CuO particles in the range of temperatures 268–271 °C,^{28,29} which is consistent with the 2–3 nm particles observed by HRTEM. After the hydrothermal step, the reduction peak of 3Cu_{HT} almost shows no shift accompanying the increase in hydrogen consumption. According to the literature, lower dispersion of CuO species results in a larger copper size, leading to higher reduction temperature in H₂-TPR.^{30,31} However, in our work, the TEM statistical results about the copper particles (Table 1) indicating the size of hydrothermal sample is close to that of the nonhydrothermal sample (2.3 and 2.0 nm for 3Cu_{HT}

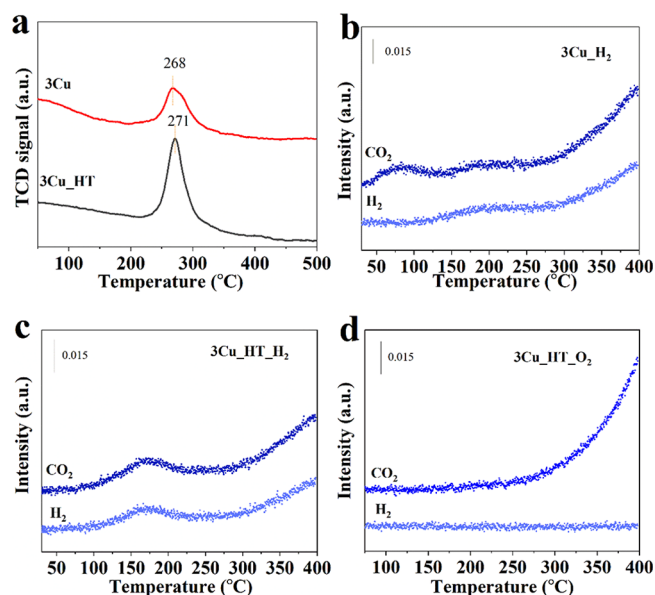


Figure 5. (a) H₂-TPR analysis of 3Cu/SiO₂. CO-TPR analysis of (b) 3Cu_{H₂}, (c) 3Cu_{HT}H₂, and (d) 3Cu_{HT}O₂.

Table 2. Dispersion of Cu (D_{Cu}), Position of the Peak of H₂-TPR (T_g), and H₂ Consumption of Samples

sample	D_{Cu} (%) ^a	T_g (°C) ^b	H ₂ (μmol·g ⁻¹) ^b	
3Cu	62	269	427 ^c	513 ^d
3Cu _{HT}	59	271	629 ^c	604 ^d

^aCalculated from N₂O chemisorption test. ^bDetermined from the H₂-TPR experiment. ^cExperimental H₂ consumption. ^dTheoretical H₂ consumption.

and 3Cu, respectively). The reduction peak after hydrothermal treatment shows almost no shift. We conjecture that the dispersion of 3Cu and 3Cu_{HT} is nearly similar. In order to verify the reliability of the above conclusions, copper dispersion was determined by N₂O chemisorption. The D values shown in Table 2 reflect 59 and 62% for 3Cu_{HT} and 3Cu, respectively, nearly the same. Hydrogen consumption is very sensitive to the conditions of catalyst preparation. The experimental hydrogen consumption (629 μmol·g⁻¹) summarized in Table 2 is roughly identical to the theoretical hydrogen consumption (604 μmol·g⁻¹) for 3Cu_{HT}, implying that all the oxygen species related to copper atoms were reduced. However, for 3Cu, the experimental hydrogen consumption (427 μmol·g⁻¹) is less than the theoretical hydrogen consumption (513 μmol·g⁻¹), giving a hint that partial copper atoms were covered and the bounded oxygen species were unavailable to be reduced by H₂. Therefore, hydrothermal treatment did not enhance the dispersion of copper but did affect the redox properties of the catalyst.

In order to further analyze the reduction properties of the catalysts, CO-TPR was performed. For 3Cu_{H₂} (Figure 5b), two small peaks at ca. 70 and 200 °C appear in the curve representing CO₂, while only a broad peak at 200 °C appears on the H₂ curve. We attributed the latter peak (ca. 200 °C) to the surface water–gas shift (WGS) reaction between the CO molecule and the hydroxyls bounded to copper,³² while the former peak (ca. 70 °C) was derived from oxidation of CO. As can be seen in Figure 5c, a broad peak of CO₂ and H₂ at 170 °C with the same trend was observed for 3Cu_{HT}H₂, which

is attributed to the favorable effect of reduction of the surface Cu hydroxyls by CO.^{32,33} Obviously, higher amounts of CO₂ and H₂ implies more copper hydroxyls. In addition, the CO-TPR profile of 3Cu_HT_O₂ is shown in Figure 5d as a comparison. The curve of CO₂ rises with increasing temperature, especially at relatively high temperatures (>300 °C), while the curve of H₂ does not fluctuate at all, which suggests that the oxygen species of the catalyst react with CO to form CO₂ at relatively high temperatures, not originated from the surface hydroxyl reduction. Obviously, no hydroxyls are involved in this process for the O₂-pretreated sample. All the above show that hydrogen pretreatment is significantly critical to generate copper hydroxyls on the surface and hydrothermal step promoted the number of hydroxyls.

The XAFS technique was used to verify the electronic and local coordination structure of the small-sized copper species. The XANES data for the Cu K edge clearly demonstrate the presence of Cu(II) in both 3Cu and 3Cu_HT (Figure 6a,

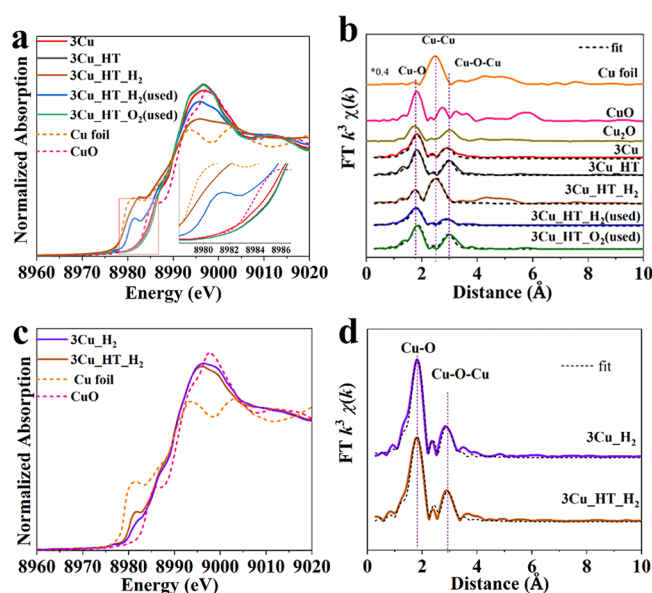


Figure 6. Cu K-edge (a) XANES profiles of 3Cu/SiO₂ samples and (b) EXAFS fitting results in the R space of 3Cu/SiO₂ samples; Cu K-edge XANES profiles (c) and EXAFS fitting results in the R space (d) of 3Cu/SiO₂ samples after stability test.

Table S1, and Figure S1). The EXAFS spectra and fitting results of Cu/SiO₂ catalysts are shown in Figure 6b and Table 3. The related EXAFS spectra for 3Cu_HT displays two peaks,

among which the first peak is at approximately 1.95 Å corresponding to the first shell of Cu–O and the second peak is at a distance of ca. 2.99 Å derived from the Cu–O–Cu structure that is different from the Cu–Cu of CuO structure at a distance of ca. 2.74 Å, indicating the low crystallinity and small size of Cu in 3Cu_HT.^{33,34} Compared with hydrothermal sample, the two shells of 3Cu show similar structure at distances of ca. 1.94 and 2.98 Å, respectively. The difference between the CN of the Cu–O shell of 3Cu and 3Cu_HT is also minor (4.0 and 3.8 for 3Cu_HT and 3Cu, respectively). Moreover, 3Cu_HT shows apparently higher intensity in the second shell with a CN of 2.8 compared to 3Cu with a CN of 1.9 (Table 3). Therefore, hydrothermal pretreatment not only affected the structure of the SiO₂ but also changed the coordination structure of copper.

As discussed above, hydrothermal treatment affected the coordination structure of the supported Cu. Furthermore, hydrogen pretreatment rather than oxygen pretreatment is a pivotal step to ensure the existence of copper hydroxyls.

3.4. Effects of Hydrothermal Processes on the Catalytic Activities on Copper–Silica Catalysts. From the light-off curve and stability test of CO oxidation, it can be seen that the hydrothermal process can improve the catalytic activity, especially the stability of the sample. The XRD results exhibit no differences on structure between 3Cu_HT and 3Cu because all the fresh samples only show the amorphous broad peaks of SiO₂. It can be seen that a very tiny peak at 37° is ascribed to the (111) crystal face of Cu₂O (JCPDS card no. 34-1354) for 3Cu_HT_H₂ (used) (Figure 2b), but the corresponding 3Cu_H₂ (used) did not contain any component of Cu₂O. Simultaneously, N₂O chemisorption, nitrogen adsorption/desorption, and TEM proved the lower BET specific surface area, similar particle size of copper, and similar dispersion of copper for 3Cu_HT compared to 3Cu. This is unusual because many studies have shown that excellent activity corresponds to high specific surface area, high dispersion, and small size because of highly unsaturated adsorbed sites and high atomic utilization.^{35,36} Therefore, we can infer that the effect of hydrothermal treatment on activity is not due to the size and dispersion of active species. However, nitrogen adsorption/desorption and TEM confirmed that hydrothermal treatment caused a great change in the morphology and structure of SiO₂ (Figures 3 and 4), as previously analyzed.

More useful information can be obtained through CO-TPR. Under hydrogen pretreatment conditions, more amount of CO₂ accompanied by H₂ appeared for 3Cu_HT compared to

Table 3. Oxidation State of Copper (δ) and Cu K-Edge EXAFS Fitting Results (R , distance; CN, coordination number; σ^2 , Debye–Waller factor^a; and ΔE_0 , inner potential correction^b of 3Cu/SiO₂ samples)

sample	δ	Cu–O		Cu–Cu		Cu–O–Cu	
		R (Å)	CN	R (Å)	CN	R (Å)	CN
3Cu	2	1.94 ± 0.01	3.8 ± 0.2			2.98 ± 0.02	1.9 ± 0.4
3Cu_HT	2	1.95 ± 0.01	4.0 ± 0.2			2.99 ± 0.01	2.8 ± 0.4
3Cu_HT_O ₂ (used)	2	1.95 ± 0.01	3.9 ± 0.3			2.99 ± 0.01	2.9 ± 0.4
3Cu_HT_H ₂ (used)	1.2	1.92 ± 0.01	2.8 ± 0.1			2.97 ± 0.02	1.3 ± 0.2
3Cu_HT_H ₂ ^c	1.4	1.92 ± 0.01	2.9 ± 0.1			2.95 ± 0.01	1.3 ± 0.3
3Cu_H ₂ ^c	1.6	1.93 ± 0.01	3.4 ± 0.2			2.99 ± 0.02	1.1 ± 0.5
3Cu_HT_H ₂	0.5	1.88 ± 0.02	1.4 ± 0.2	2.54 ± 0.01	3.8 ± 0.3		

^a $\sigma^2 = 0.008 \text{ \AA}^2$ for Cu–Cu shells and 0.003 or 0.0045 \AA^2 for Cu–O (3Cu_HT_H₂ only) or Cu–O (except 3Cu_HT_H₂), respectively. ^b $\Delta E_0 = 11.5 \pm 0.5 \text{ eV}$ for all samples except 3Cu_HT_H₂; $5.5 \pm 1.6 \text{ eV}$ for 3Cu_HT_H₂. ^cAfter stability test.

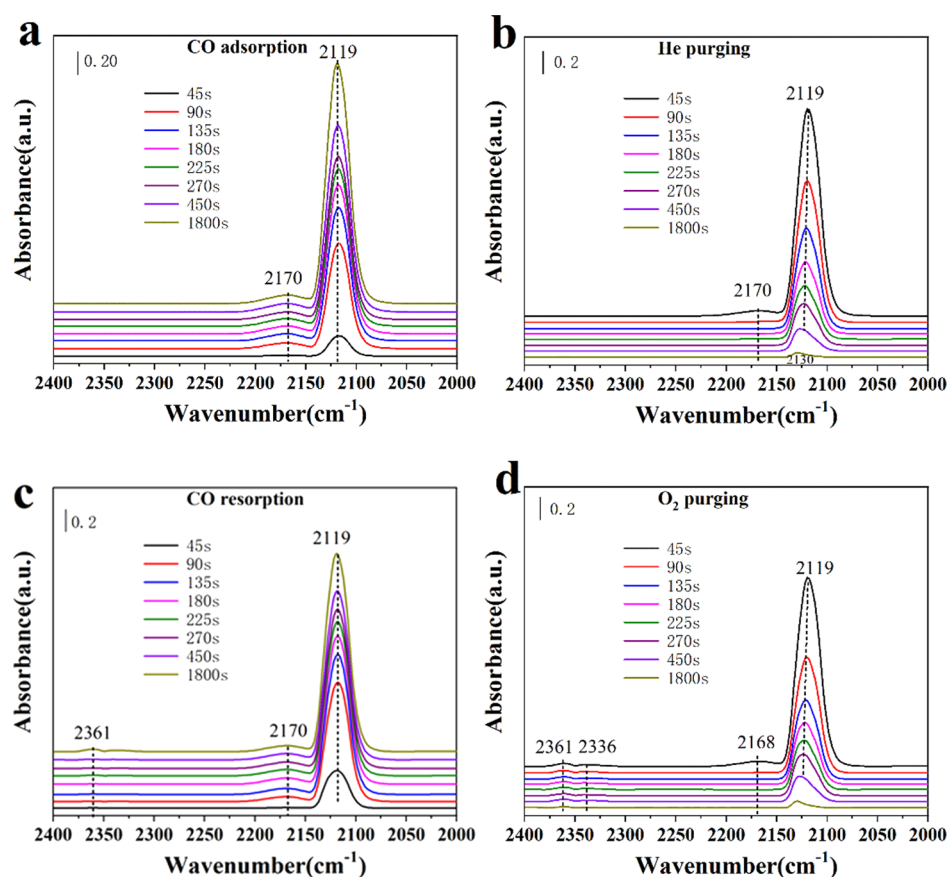


Figure 7. In situ DRIFTS study for 3Cu_HT tested at 30 °C pretreated with 5% H₂ at 300 °C.

3Cu (see Figure 5b,c), implying that more copper hydroxyls appeared on the 3Cu_HT surface. As discussed above, the participation of copper hydroxyls can explain the simultaneous formation of H₂ and CO₂. In this study, interestingly, the higher the Cu–OH contents, the better the CO oxidation activity of the catalyst, revealing the importance of copper hydroxyls. Before commenting on these results, let us recall that the H₂-TPR profiles of Cu/SiO₂ catalysts appeared regularly on the conditions of catalyst preparation. The samples contain a significantly higher amount of Cu oxide species after hydrothermal process at 200 °C for 24 h, resulting in more hydrogen consumption in 3Cu_HT than 3Cu on H₂-TPR (Figure 5a and Table 2). Therefore, more copper hydroxyls were present in the hydrothermal pretreatment catalyst after hydrogen pretreatment.

The results of XANES analysis show that the oxidation states of copper for 3Cu_HT and 3Cu after stability test are 1.4 and 1.6, respectively (Figure 6c, Tables 3, S1, and Figure S1), indicating that the sample without hydrothermal step is more susceptible to be oxidized. Compared with 3Cu_HT_H₂ (used) of the identical oxidation state of 1.2, the copper oxidation state after stability test was increased, revealing that copper was gradually oxidized during the CO oxidation reaction. This could be the reason for the gradual deactivation of catalysts. The related EXAFS spectrum for samples after stability tests also displays two shells as fresh samples, while the CN of the two shells reduced compared to fresh samples. As for Cu–O shell, 3Cu_HT and 3Cu after stability test shows a CN of 2.9 and 3.4, respectively. The CN of Cu–O–Cu is 1.3 and 1.4 for 3Cu_HT and 3Cu after the stability test, respectively. We found that the CNs of the hydrothermal

sample decrease more than the nonhydrothermal sample compared to the fresh sample, which shows that more copper hydroxyls involved in the stability test for hydrothermal samples.

In order to gain further insights into the chemical adsorption properties of the catalysts, the in situ DRIFTS measurements were carried out for Cu/SiO₂ catalysts in a “CO–He–CO–O₂” mode at 30 °C during the CO adsorption. No peaks were found on the spectral ranges of 2200–2140 and 2100–2000 cm⁻¹, attributing to CO adsorption on Cu²⁺ and Cu⁰ sites, respectively, indicating the minor Cu²⁺ and Cu⁰ species on the surface of Cu/SiO₂ catalysts. For 3Cu_HT_H₂ (Figure 7a), the IR bands at 2119 and 2170 cm⁻¹ can be attributed to linear CO adsorbed on Cu⁺ sites (Cu⁺–CO) and gaseous CO, respectively.³⁷ As for 3Cu_H₂, the same Cu⁺–CO species at 2121 cm⁻¹ was accompanied by gaseous CO at 2170 cm⁻¹ (Figure 8a). However, the related intensity was lower, revealing the lower adsorption of CO on Cu(I) species for 3Cu_H₂. During the He-purging process, the carbonyl peak gradually weakened and continued to decay up to 1800 s for both 3Cu_HT and 3Cu (Figures 7b and 8b). Simultaneously, the apparent continuous blue shift of the carbonyl up to 1800 s at 2130 cm⁻¹ in this process is similar to the blue shift of the peak after O₂ introduced (Figures 7d, 8d). With the purging of He, the concentration of CO decreases and the reducibility of copper species becomes weaker, which likely result in a blue shift of this peak. During subsequent CO readsorption (Figures 7c, 8c), the Cu⁺–CO peaks show a red shift and reach a steady position quickly around 90 s. After the gas channel was switched to 1% O₂/N₂ (Figures 7d, 8d), the peak in the collected spectra showed a blue shift character similar to that in

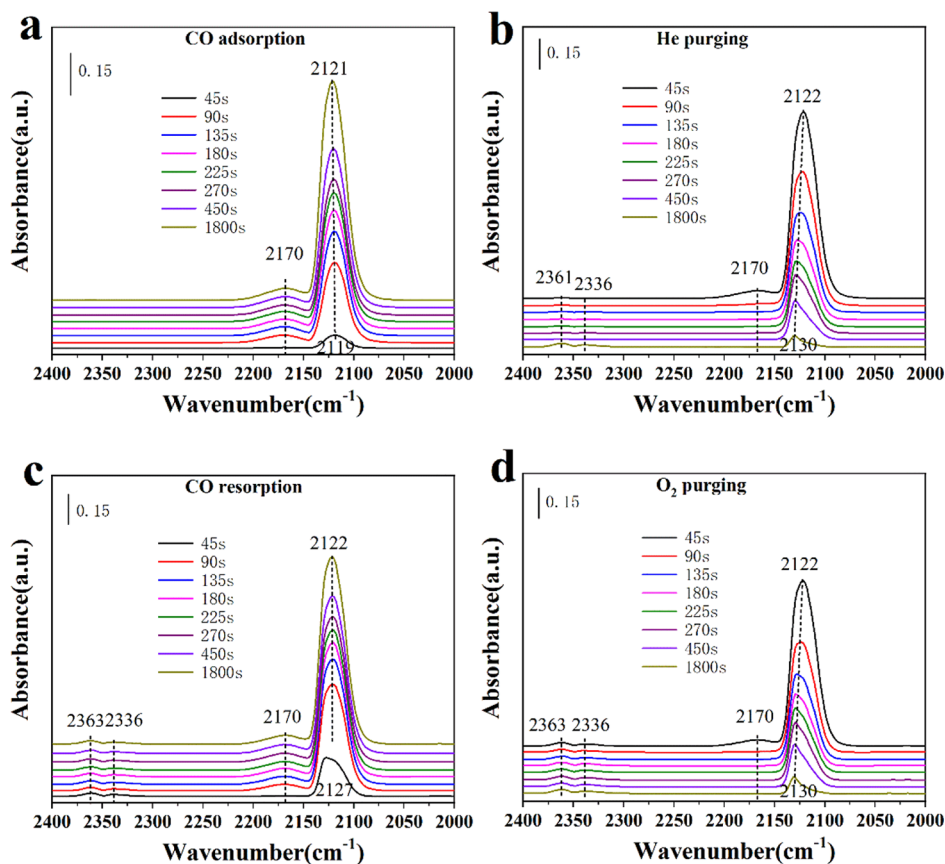


Figure 8. In situ DRIFTS study for 3Cu tested at 30 °C pretreated with 5% H₂ at 300 °C.

the He-purging process, which can be taken as oxidation of Cu⁺. In addition, the peaks at ca. 2363 and 2336 cm⁻¹ are attributed to the adsorption gas-phase CO₂ because of the reaction of the adsorbed CO with O₂. The spectral range of 3800–3550 cm⁻¹ of the CO adsorption step was analyzed (Figure 9). 3735 and 3650 cm⁻¹ are typical for Si–OH and Cu–OH,^{38,39} respectively, which gradually strengthened from 45 to 1800 s. 3Cu and 3Cu_{HT} after hydrogen pretreatment show the Si–OH and Cu–OH with different peak intensities (Figure 9a,b,d). 3Cu_{HT} shows a stronger peak intensity, indicating that there are more copper hydroxyls on the surface of 3Cu_{HT} than 3Cu, which is consistent with the result of CO-TPR.

After calcination in air at 400 °C for 4 h, no copper hydroxyls remain on the surface of 3Cu_{HT}, which can be proved by CO-TPR and DRIFTS of 3Cu_{HT}-O₂ (Figures 5d, 9c). We infer that the copper hydroxyls are absent on 3Cu_{HT}. However, the results of H₂-TPR, CO-TPR, and in situ DRIFTS prove that there are more Cu–OH and stronger adsorption capacity for CO in 3Cu_{HT}-H₂ than 3Cu_{H₂}. The results of XAFS give a hint that there are more active sites for 3Cu_{HT} than 3Cu (Figure 6b and Table 3). In addition, the modification of the catalyst structure by the hydrothermal step is proved by nitrogen adsorption/desorption (Figure 3a,b and Table 1), TEM (Figure 4a,c), and XAFS (Figure 6a,b and Table 3). The modification of the catalyst coordination structure after hydrothermal step results in 3Cu_{HT}-H₂, exhibiting stronger adsorption capacity and more copper hydroxyls, and 3Cu_{HT} showing more active sites, which leads to better stability of CO oxidation on 3Cu_{HT}-H₂. In other words, the better catalytic performance for a hydro-

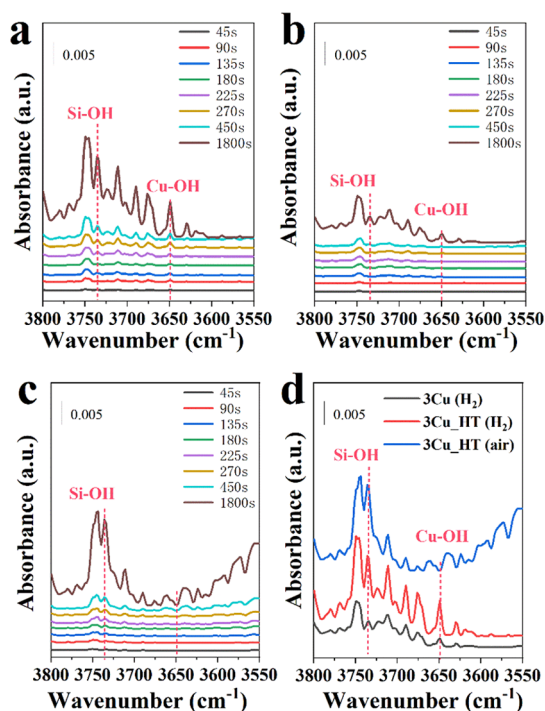
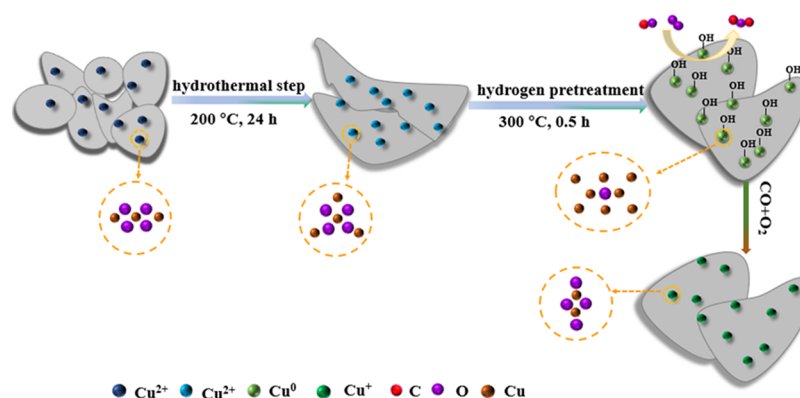


Figure 9. In situ DRIFTS study for (a) 3Cu_{HT} pretreated with 5% H₂, (b) 3Cu pretreated with 5% H₂ and (c) 3Cu_{HT} pretreated with compressed air (pretreatment conditions, 300 °C, test conditions, 30 °C, 2% CO/He).

Scheme 1. Illustration of the Structure Transformation of 3Cu/SiO₂

thermal catalyst than a nonhydrothermal catalyst results from the more available active copper hydroxyl species benefitting from a more stable coordination structure, providing more non-inactivated active sites for subsequent adsorption and reaction processes. The structure transformation of Cu/SiO₂ catalyst is described in Scheme 1. After hydrothermal treatment, 3Cu underwent the reconstruction of SiO₂ and the coordination structure of copper to form 3Cu_{HT}.

3.5. Effects of H₂ Pretreatment on the Catalytic Activities of Copper–Silica Catalysts. The sample after the hydrogen pretreatment showed much higher activity compared with the sample after the oxygen pretreatment (Figure 1a), which is consistent with recent studies about copper-based catalysts for CO oxidation, confirming that the low oxidation state of copper obtained by reduction pretreatment is more conducive to CO oxidation than high oxidation state of copper obtained by oxidation pretreatment.^{6,7} The oxygen-pretreated samples showed very limited CO conversion, expressing less than 10% up to 300 °C (Figure 1a). 3Cu_{HT} was subjected to explore the reason for the effects of different pretreatment atmospheres on catalytic activity.

The XRD patterns of the used catalysts in Figure 2b reveal that no crystallized Cu phase was generated for 3Cu_{HT}_O₂ (used), while a tiny peak of Cu₂O was shown in 3Cu_{HT}_H₂ (used). The used sample of 3Cu_{HT} showed a similar size of copper with the fresh catalyst in Figure 4 and Table 1 (2.5, 2.4, and 2.3 nm for 3Cu_{HT}_H₂ (used), 3Cu_{HT}_O₂ (used), and 3Cu_{HT}, respectively). Furthermore, the particle size of used catalysts after hydrogen pretreatment and oxygen pretreatment were almost the same (Figure 4f,h and Table 1). However, after the catalyst underwent CO oxidation, the size of SiO₂ became significantly larger (Figure 4e,g). Although it is still an amorphous structure, it can be seen that the SiO₂ fusion is more thorough.

As the abovementioned results, comparing the CO-TPR results of 3Cu_{HT} after different pretreatments, it can be seen that the only H₂ peak generated after hydrogen pretreatment rather than oxygen pretreatment. Simultaneous production of CO₂ and H₂ in CO-TPR indicates that copper hydroxyl groups are involved in the reaction process, and these copper hydroxyls completely disappeared after O₂ pretreatment. In other words, oxygen pretreatment failed to produce copper hydroxyls, which resulted in less activity, while hydrogen pretreatment is the decisive step to produce surface copper hydroxyls. Guo et al. found that copper hydroxyl species tend to promote the formation of CO₂.³³ Tang group found that the surface hydroxyls could promote CO oxidation by the

chemisorption of gaseous CO, resulting in increasing the CO concentration around the Cu active sites via synthesizing a hydroxyl-group-rich SiO₂–AlOOH nanosheets-supported CuO catalyst.⁴⁰ Jia group found the significance of bridged surface OH for WGS reaction.¹⁸ It can be seen that the surface hydroxyls contribute significantly to the oxidation of carbon monoxide.

In order to further study the effects of different gas pretreatments on the catalyst, the test results of XAFS of used samples have been analyzed. The oxidation states of 3Cu_{HT}_O₂ (used) and 3Cu_{HT}_H₂ (used) were determined as Cu(II) (Figure 6a, Table 3). Interestingly, the line shapes of 3Cu_{HT}_O₂ (used) were almost identical to the corresponding fresh sample, implying that O₂-pretreated catalysts were hardly affected by the CO oxidation gas. The related EXAFS fitting results are summarized in Table 3, showing that all the investigated samples after CO reaction contain the Cu–O and Cu–O–Cu shells as fresh samples. Unsurprisingly, 3Cu_{HT}_O₂ (used) exhibit the EXAFS spectrum and fitting result that is similar to 3Cu_{HT} (Figure 6b and Table 3). The progress of catalytic reaction indispensably requires both the adsorption of reactants and the desorption of products. The adsorption and desorption of gas on the catalyst inevitably affect the electronic structure and local coordination structure of the catalyst, which can be characterized and embodied by the XAFS spectrum. Therefore, we can speculate that the catalysts after oxygen pretreatment had very weak adsorption to reactant gases or do not adsorb at all, which reflects extremely poor catalytic activity for CO oxidation. Considering that the fresh sample was obtained by calcinating in air, we believe that 3Cu_{HT}_O₂ should not be different from 3Cu_{HT}. After the 3Cu_{HT} was treated with 5% H₂/Ar gas for 30 min in a tube with needle valves at both ends, it was compressed into a slice in a glove box filled with N₂ and then sealed with a Kapton tape. The results of 3Cu_{HT}_H₂ are summarized in Figure 6 and Table 3. For XANES of 3Cu_{HT}_H₂ (Figure 6a), the result demonstrates a reduced feature with a valence of 0.5, indicating that the sample mixes bulk metallic copper and a small part of surface-oxidized copper. It can be concluded from the EXAFS results of 3Cu_{HT}_H₂ that the best-fitted shells of Cu–O and Cu–Cu are shown in ca. 1.88 and 2.54 Å, respectively. The Cu–Cu shell demonstrates high intensity with a CN of 3.8, while the Cu–O shell shows a CN of 1.4. As for 3Cu_{HT}_H₂(used), the line shapes on XANES is very different from that of the corresponding fresh sample with a valence state of 1.2 obtained by the linear combination fit, implying that the different

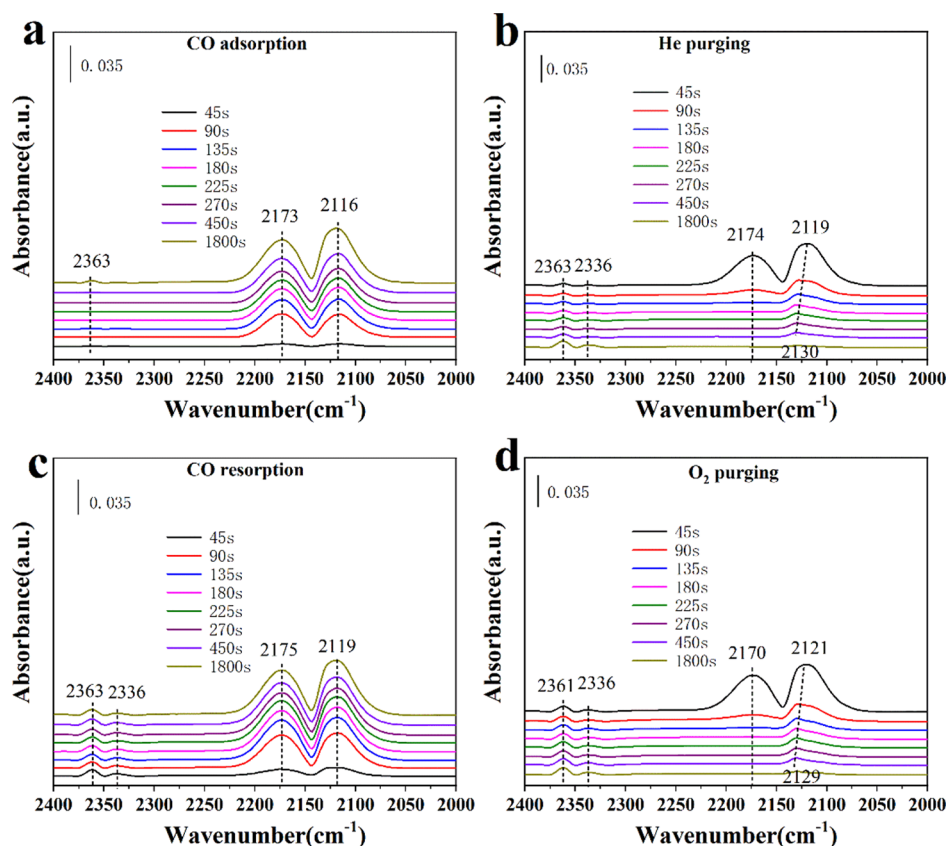


Figure 10. In situ DRIFTS study for 3Cu_HT tested at 30 °C pretreated with compressed air at 300 °C.

coordination structure of Cu after CO oxidation and Cu was oxidized partly during CO oxidation reaction. As for the EXAFS result of 3Cu_HT_H₂(used), a prominent peak was exhibited at ca. 1.92 Å, originating from the first shell of Cu–O contribution with a CN of 2.8 and prominent peak at ca. 2.97 Å, originating from the second shell of Cu–O–Cu contribution with a CN of 1.3, which is much lower than the CN of the fresh sample.

In situ DRIFTS was used to further demonstrate the adsorption capacity of the catalyst. The IR spectrum of 3Cu_HT_O₂ is shown in Figure 10 with a range of 2100–2400 cm⁻¹ in a “CO–He–CO–O₂” mode at 30 °C. During the CO adsorption process, 2173 and 2116 cm⁻¹ with similar intensity represent CO gas and Cu⁺–CO, respectively. Clearly, there are almost no Cu⁺ ions present, which is 1 order of magnitude lower compared with the Cu⁺–CO intensity of 3Cu_HT_H₂ (Figure 7a).^{41,42} It is conceivable that copper was oxidized after oxygen pretreatment proved by XAFS. In addition, the very weak intensity of the Cu⁺–CO peak proves the extremely weak adsorption of CO in the catalyst with the air pretreatment, which is also evidenced by XAFS analysis. The absence of Cu²⁺–CO (CO adsorption on Cu²⁺) peak is due to the low copper content (3 wt % Cu) and the weak ability of Cu²⁺ to adsorb CO.⁴² It was found that the CO adsorption of the H₂-pretreated sample is significantly stronger than that of O₂-pretreated samples. Furthermore, Cu–OH is absent at 3650 cm⁻¹ for 3Cu_HT after oxidation pretreatment (Figure 9c,d), despite the strong Si–OH peak at 3735 cm⁻¹, which not only negates the contribution of Si–OH to catalytic activity of CO oxidation but also proves the importance of Cu–OH.

As a conclusion from CO-TPR, XAFS, in situ DRIFTS, and TPR investigation, we pointed out that hydrogen pretreatment not only reduced copper but also provided a decisive condition to produce copper hydroxyl active species, leading to more favorable adsorption of CO, resulting in high activity for CO oxidation. The structure transformation of Cu/SiO₂ catalyst is described in Scheme 1, which shows that the generation of surface copper hydroxyls is entirely due to the hydrogen pretreatment. However, oxygen pretreatment was unable to generate surface copper hydroxyls. As a result, the O₂-pretreated catalysts are more difficult to adsorb the reaction gas and produce unexpectedly low activity. In short, hydrogen pretreatment is essential for achieving a highly active CO oxidation reaction.

4. CONCLUSIONS

In this work, small-sized Cu particles (average particle size of 2–3 nm) on silica support were synthesized by a modified deposition–precipitation method. The catalytic stability of the catalyst after the hydrothermal step was improved for the CO oxidation reaction. Full structural characterization revealed that the catalyst with H₂ pretreatment exhibited much higher activity in comparison to that with O₂ pretreatment. The hydrogen pretreatment process can reduce the oxidation state of copper and provide a sufficient and decisive condition to produce copper hydroxy active species, resulting in the prodigious activity compared to oxygen-pretreated samples. The hydrothermal step induced a great change of the texture structure of SiO₂ and the coordination structure of copper, resulting in stabilizing the catalytic environment that is conducive to the production of more active copper hydroxyls.

In brief, this work describes the important role of hydrogen pretreatment for the generation of surface copper hydroxyls and the significance of surface copper hydroxyls for the CO oxidation reaction.

ASSOCIATED CONTENT

Supporting Information

The Supporting Information is available free of charge at <https://pubs.acs.org/doi/10.1021/acs.jpcc.0c07072>.

Determination of the oxidation state of Cu and molar proportion of Cu⁰ and Cu²⁺ (PDF)

AUTHOR INFORMATION

Corresponding Authors

Chun-Jiang Jia – Key Laboratory for Colloid and Interface Chemistry, Key Laboratory of Special Aggregated Materials, School of Chemistry and Chemical Engineering, Shandong University, Jinan 250100, China; orcid.org/0000-0002-4254-5100; Email: jiaj@sdu.edu.cn

Rui Si – Shanghai Synchrotron Radiation Facility, Shanghai Institute of Applied Physics, Chinese Academy of Sciences, Shanghai 201204, China; orcid.org/0000-0003-0732-9688; Email: sirui@sinap.ac.cn

Authors

Miao-Miao Wang – Shanghai Synchrotron Radiation Facility, Shanghai Institute of Applied Physics, Chinese Academy of Sciences, Shanghai 201204, China; University of Chinese Academy of Sciences, Beijing 100049, China

Jing Yu – Shanghai Institute of Measurement and Testing Technology, Shanghai 200233, China

Wei-Wei Wang – Key Laboratory for Colloid and Interface Chemistry, Key Laboratory of Special Aggregated Materials, School of Chemistry and Chemical Engineering, Shandong University, Jinan 250100, China

Jun-Xiang Chen – Division of China, TILON Group Technology Limited, Shanghai 200090, China

Complete contact information is available at: <https://pubs.acs.org/doi/10.1021/acs.jpcc.0c07072>

Notes

The authors declare no competing financial interest.

ACKNOWLEDGMENTS

This work was financially supported by the National Science Foundation of China (grant nos 21773288, 21771117, and 21805167), the National Key Basic Research Program of China (2017YFA0403402), the Doctoral Fund from the Science Foundation of Shandong Province of China (grant no. ZR2018BB010), and the Shanghai Large Scientific Facilities Center. We thank Dr. Shuangquan Hu (Evonik Industries) for his kind help on supply of high surface area silica support and the Center of Structural Characterizations and Property Measurements at Shandong University for the help on sample characterizations.

REFERENCES

(1) Wang, X.-L.; Fu, X.-P.; Wang, W.-W.; Ma, C.; Si, R.; Jia, C.-J. Effect of Structural Evolution of Gold Species Supported on Ceria in Catalyzing CO Oxidation. *J. Phys. Chem. C* **2019**, *123*, 9001–9012.

(2) Kahlich, M. J.; Gasteiger, H. A.; Behm, R. J. Kinetics of the Selective CO Oxidation in H₂-Rich Gas on Pt/Al₂O₃. *J. Catal.* **1997**, *171*, 93–105.

(3) Okumura, M.; Masuyama, N.; Konishi, E.; Ichikawa, S.; Akita, T. CO Oxidation below Room Temperature over Ir/TiO₂ Catalyst Prepared by Deposition Precipitation Method. *J. Catal.* **2002**, *208*, 485–489.

(4) Wang, W.-W.; Yu, W.-Z.; Du, P.-P.; Xu, H.; Jin, Z.; Si, R.; Ma, C.; Shi, S.; Jia, C.-J.; Yan, C.-H. Crystal Plane Effect of Ceria on Supported Copper Oxide Cluster Catalyst for CO Oxidation: Importance of Metal–Support Interaction. *ACS Catal.* **2017**, *7*, 1313–1329.

(5) Jansson, J. Low-Temperature CO Oxidation over Co₃O₄/Al₂O₃. *J. Catal.* **2000**, *194*, 55–60.

(6) Xu, F.; Mudiyansele, K.; Baber, A. E.; Soldemo, M.; Weissenrieder, J.; White, M. G.; Stacchiola, D. J. Redox-Mediated Reconstruction of Copper during Carbon Monoxide Oxidation. *J. Phys. Chem. C* **2014**, *118*, 15902–15909.

(7) Gonçalves, R. V.; Wojcieszak, R.; Wender, H.; Dias, C. S. B.; Vono, L. L. R.; Eberhardt, D.; Teixeira, S. R.; Rossi, L. M. Easy Access to Metallic Copper Nanoparticles with High Activity and Stability for CO Oxidation. *ACS Appl. Mater. Interfaces* **2015**, *7*, 7987–7994.

(8) Zhao, F.; Ji, S.; Wu, P.; Li, Z.; Li, C. Catalytic Oxidation of CO over Cu_xCe_{1-x}O_{2-x}/SBA-15/FeCrAl Monolithic Catalysts. *Catal. Today* **2009**, *147*, S215–S219.

(9) Eren, B.; Heine, C.; Bluhm, H.; Somorjai, G. A.; Salmeron, M. Catalyst Chemical State during CO Oxidation Reaction on Cu (111) Studied with Ambient Pressure XPS and NEXAFS. *J. Am. Chem. Soc.* **2015**, *137*, 11186–11190.

(10) Sadykov, V. A.; Tikhov, S. F.; Bulgakov, N. N.; Gerasov, A. P. Catalytic Oxidation of CO on CuO_x Revisited: Impact of the Surface State on the Apparent Kinetic Parameters. *Catal. Today* **2009**, *144*, 324–333.

(11) Feng, Y.; Zheng, X. Plasma-Enhanced Catalytic CuO Nanowires for CO Oxidation. *Nano Lett.* **2010**, *10*, 4762–4766.

(12) Liu, X.; Wang, A.; Li, L.; Zhang, T.; Mou, C.-Y.; Lee, J.-F. Structural Changes of Au–Cu Bimetallic Catalysts in CO Oxidation: In Situ XRD, EPR, XANES, and FT-IR Characterizations. *J. Catal.* **2011**, *278*, 288–296.

(13) Zhou, K.; Wang, R.; Xu, B.; Li, Y. Synthesis, Characterization and Catalytic Properties of CuO Nanocrystals with Various Shapes. *Nanotechnology* **2006**, *17*, 3939–3943.

(14) Yang, Z.; He, B.; Lu, Z.; Hermansson, K. Physisorbed, Chemisorbed, and Oxidized CO on Highly Active Cu–CeO₂(111). *J. Phys. Chem. C* **2010**, *114*, 4486–4494.

(15) Yang, F.; Graciani, J.; Evans, J.; Liu, P.; Hrbek, J.; Sanz, J. F.; Rodriguez, J. A. CO Oxidation on Inverse CeO_x/Cu (111) Catalysts: High Catalytic Activity and Ceria-Promoted Dissociation of O₂. *J. Am. Chem. Soc.* **2011**, *133*, 3444–3451.

(16) Yao, S.; Mudiyansele, K.; Xu, W.; Johnston-Peck, A. C.; Senanayake, S. D. Unraveling the Dynamic Nature of a CuO/CeO₂ Catalyst for CO Oxidation in Operando: A Combined Study of XANES (Fluorescence) and DRIFTS. *ACS Catal.* **2014**, *4*, 1650–1661.

(17) Tu, C.-H.; Wang, A.-Q.; Zheng, M.-Y.; Wang, X.-D.; Zhang, T. Factors Influencing the Catalytic Activity of SBA-15-Supported Copper Nanoparticles in CO Oxidation. *Appl. Catal., A* **2006**, *297*, 40–47.

(18) Fu, X.-P.; Guo, L.-W.; Wang, W.-W.; Ma, C.; Jia, C.-J.; Wu, K.; Si, R.; Sun, L.-D.; Yan, C.-H. Direct Identification of Active Surface Species for the Water-Gas Shift Reaction on a Gold-Ceria Catalyst. *J. Am. Chem. Soc.* **2019**, *141*, 4613–4623.

(19) Nan, B.; Hu, X.-C.; Wang, X.; Jia, C.-J.; Ma, C.; Li, M.-X.; Si, R. Effects of Multiple Platinum Species on Catalytic Reactivity Distinguished by Electron Microscopy and X-ray Absorption Spectroscopy Techniques. *J. Phys. Chem. C* **2017**, *121*, 25805–25817.

(20) Ma, L.; Cheng, Y.; Cavataio, G.; McCabe, R. W.; Fu, L.; Li, J. Characterization of Commercial Cu-SSZ-13 and Cu-SAPO-34

Catalysts with Hydrothermal Treatment for NH₃-SCR of NO_x in Diesel Exhaust. *Chem. Eng. J.* **2013**, *225*, 323–330.

(21) Mao, D.-S.; Guo, Q.-S.; Meng, T.; Lu, G.-Z. Effect of Hydrothermal Treatment on the Acidity and Catalytic Performance of Nanosized HZSM-5 Zeolites for the Conversion of Methanol to Propene. *Acta Phys.-Chim. Sin.* **2010**, *26*, 338–344.

(22) Mironenko, R. M.; Belskaya, O. B.; Talsi, V. P.; Gulyaeva, T. I.; Kazakov, M. O.; Nizovskii, A. I.; Kalinkin, A. V.; Bukhtiyarov, V. I.; Lavrenov, A. V.; Likholobov, V. A. Effect of γ -Al₂O₃ Hydrothermal Treatment on the Formation and Properties of Platinum Sites in Pt/ γ -Al₂O₃ Catalysts. *Appl. Catal., A* **2014**, *469*, 472–482.

(23) Yang, D.; Guo, G.; Hu, J.; Wang, C.; Jiang, D. Hydrothermal Treatment to Prepare Hydroxyl Group Modified Multi-Walled Carbon Nanotubes. *J. Mater. Chem.* **2008**, *18*, 350–354.

(24) Chiriac, A.; Dragoi, B.; Ungureanu, A.; Ciotonea, C.; Mazilu, I.; Royer, S.; Mamede, A. S.; Rombi, E.; Ferino, I.; Dumitriu, E. Facile Synthesis of Highly Dispersed and Thermally Stable Copper-Based Nanoparticles Supported on SBA-15 Occluded with P123 Surfactant for Catalytic Applications. *J. Catal.* **2016**, *339*, 270–283.

(25) Sietsma, J. R. A.; Meeldijk, J. D.; Versluijs-Helder, M.; Broersma, A.; van Dillen, A. J.; de Jongh, P. E.; de Jong, K. P. Ordered Mesoporous Silica to Study the Preparation of Ni/SiO₂ Ex Nitrate Catalysts: Impregnation, Drying, and Thermal Treatments. *Chem. Mater.* **2008**, *20*, 2921–2931.

(26) Zhao, D.; Feng, J. L.; Huo, Q. S.; Melosh, N.; Fredrickson, G. H.; Chmelka, B. F.; Stucky, G. D. Triblock Copolymer Syntheses of Mesoporous Silica with Periodic 50 to 300 Angstrom Pores. *Science* **1998**, *279*, 548–552.

(27) Groen, J. C.; Peffer, L. A. A.; Pérez-Ramírez, J. Pore Size Determination in Modified Micro- and Mesoporous Materials. Pitfalls and Limitations in Gas Adsorption Data Analysis. *Microporous Mesoporous Mater.* **2003**, *60*, 1–17.

(28) Wen, C.; Yin, A.; Cui, Y.; Yang, X.; Dai, W.-L.; Fan, K. Enhanced Catalytic Performance for SiO₂-TiO₂ Binary Oxide Supported Cu-Based Catalyst in the Hydrogenation of Dimethylxalate. *Appl. Catal., A* **2013**, *458*, 82–89.

(29) Valero, J. M.; Obregón, S.; Colón, G. Active Site Considerations on the Photocatalytic H₂ Evolution Performance of Cu-Doped TiO₂ Obtained by Different Doping Methods. *ACS Catal.* **2014**, *4*, 3320–3329.

(30) Zheng, X.-C.; Wu, S.-H.; Wang, S.-P.; Wang, S.-R.; Zhang, S.-M.; Huang, W.-P. The Preparation and Catalytic Behavior of Copper–Cerium Oxide Catalysts for Low-Temperature Carbon Monoxide Oxidation. *Appl. Catal., A* **2005**, *283*, 217–223.

(31) Liu, Z.; Amiridis, M. D.; Chen, Y. Characterization of CuO Supported on Tetragonal ZrO₂ Catalysts for N₂O Decomposition to N₂. *J. Phys. Chem. B* **2005**, *109*, 1251–1255.

(32) Si, R.; Raitano, J.; Yi, N.; Zhang, L.; Chan, S.-W.; Flytzani-Stephanopoulos, M. Structure Sensitivity of the Low-Temperature Water-Gas Shift Reaction on Cu–CeO₂ Catalysts. *Catal. Today* **2012**, *180*, 68–80.

(33) Guo, L.-L.; Yu, J.; Shu, M.; Shen, L.; Si, R. Silicon Nitride as a New Support for Copper Catalyst to Produce Acrolein via Selective Oxidation of Propene with Very Low CO₂ Release. *J. Catal.* **2019**, *380*, 352–365.

(34) Liu, A.; Liu, L.; Cao, Y.; Wang, J.; Si, R.; Gao, F.; Dong, L. Controlling Dynamic Structural Transformation of Atomically Dispersed CuO_x Species and Influence on Their Catalytic Performances. *ACS Catal.* **2019**, *9*, 9840–9851.

(35) Jones, J.; Xiong, H.; DeLaRiva, A. T.; Peterson, E. J.; Pham, H.; Challa, S. R.; Qi, G.; Oh, S.; Wiebenga, M. H.; Pereira Hernandez, X. I.; Wang, Y.; Datye, A. K. Thermally Stable Single-Atom Platinum-on-Ceria Catalysts via Atom Trapping. *Science* **2016**, *353*, 150–154.

(36) Liu, J. Catalysis by Supported Single Metal Atoms. *ACS Catal.* **2017**, *7*, 34–59.

(37) Zhang, X.-m.; Tian, P.; Tu, W.; Zhang, Z.; Xu, J.; Han, Y.-F. Tuning the Dynamic Interfacial Structure of Copper–Ceria Catalysts by Indium Oxide during CO Oxidation. *ACS Catal.* **2018**, *8*, 5261–5275.

(38) Song, J.; Wang, Y.; Walter, E. D.; Washton, N. M.; Mei, D.; Kovarik, L.; Engelhard, M. H.; Proding, S.; Wang, Y.; Peden, C. H. F.; Gao, F. Toward Rational Design of Cu/SSZ-13 Selective Catalytic Reduction Catalysts: Implications from Atomic-Level Understanding of Hydrothermal Stability. *ACS Catal.* **2017**, *7*, 8214–8227.

(39) Lezcano-Gonzalez, I.; Deka, U.; Arstad, B.; Van Yperen-De Deyne, A.; Hemelsoet, K.; Waroquier, M.; Van Speybroeck, V.; Weckhuysen, B. M.; Beale, A. M. Determining the Storage, Availability and Reactivity of NH₃ within Cu-Chabazite-Based Ammonia Selective Catalytic Reduction Systems. *Phys. Chem. Chem. Phys.* **2014**, *16*, 1639–1650.

(40) Yan, Z.; Yang, H.; Ouyang, J.; Tang, A. In Situ Loading of Highly-Dispersed CuO Nanoparticles on Hydroxyl-Group-Rich SiO₂-ALOOH Composite Nanosheets for CO Catalytic Oxidation. *Chem. Eng. J.* **2017**, *316*, 1031–1046.

(41) Liu, L.; Gao, F.; Zhao, H.; Li, Y. Tailoring Cu valence and oxygen vacancy in Cu/TiO₂ catalysts for enhanced CO₂ photo-reduction efficiency. *Appl. Catal., B* **2013**, *134–135*, 349–358.

(42) Hanukovich, S.; Dang, A.; Christopher, P. Influence of Metal Oxide Support Acid Sites on Cu-Catalyzed Nonoxidative Dehydrogenation of Ethanol to Acetaldehyde. *ACS Catal.* **2019**, *9*, 3537–3550.